

EXPLORING NUCLEAR EXOTICA AT THE LIMITS*

A.V. AFANASJEV, S.E. AGBEMAVA, A. TANINAH

Department of Physics and Astronomy, Mississippi State University
MS 39762, USA*(Received January 28, 2020)*

The study of nuclear limits has been performed and new physical mechanisms and exotic shapes allowing the extension of nuclear landscape beyond the commonly accepted boundaries have been established. The transition from ellipsoidal-to-toroidal shapes plays a critical role in potential extension of nuclear landscape to hyperheavy nuclei. Rotational excitations leading to the birth of particle (proton or neutron) bound rotational bands provide a mechanism for an extension of nuclear landscape beyond spin-zero proton and neutron drip lines.

DOI:10.5506/APhysPolBSupp.13.347

1. Introduction

The studies of the nuclei at the limits are guided by human curiosity, by the need to understand new physical mechanisms governing nuclear systems in these extreme conditions and by the demand for nuclear input in nuclear astrophysics. There is the set of the questions related to the physics at the limits listed below which looks deceivably simple but extremely difficult to answer. These questions are: What are the limits of the existence of nuclei? What are the highest proton number Z at which the nuclear landscape and periodic table of chemical elements cease to exist? What are the positions of proton and neutron drip lines? Are there some physical mechanisms which allow to extend the nuclear landscape beyond spin-zero limits? What type of nuclear shapes dominate these extremes of nuclear landscape?

Over recent years, our group has undertaken a systematic efforts in the studies of these questions within the framework of covariant density functional theory (CDFT) [1]. The analysis of Refs. [2–4] performed with three major classes of covariant energy density functionals (CEDF) has allowed

* Presented at the XXVI Nuclear Physics Workshop *Key problems of nuclear physics*, Kazimierz Dolny, Poland, September 24–29, 2019.

to evaluate the global performance of these functionals in the description of the ground-state properties of even–even nuclei. In addition, it permitted to estimate systematic uncertainties [5] in their description and the propagation of these uncertainties on approaching nuclear limits for the $Z \leq 106$ nuclei. Moreover, such an analysis has allowed to estimate theoretical uncertainties in the predictions of the two-proton and two-neutron drip lines for the $Z \leq 120$ nuclei (see Refs. [2, 3, 6]) and compare them with those obtained in non-relativistic theories (see Refs. [3, 7]). Note that in the CDFT, statistical uncertainties emerging from the details of the fitting protocol are significantly smaller than systematic ones originating from the choice of the form of the functional [8]. This is contrary to the case of non-relativistic Skyrme energy density functionals in which these two types of uncertainties are comparable at nuclear limits [7, 9].

These results formed the basis for a subsequent analysis of the extension of nuclear landscape to hyperheavy nuclei [10, 11], the study of the properties of toroidal hyperheavy nuclei [10, 11] and the discovery of new mechanism of the extension of nuclear landscape beyond spin-zero limit by means of rotational excitations [12]. In the present paper, they will be briefly reviewed and, in addition, will be supplemented by new results.

The paper is organized as follows. Section 2 is dedicated to the discussion of toroidal shapes in hyperheavy nuclei. The impact of rotational excitations on the boundaries of nuclear landscape and underlying physical mechanism are considered in Sect. 3. Finally, the summary is presented in Sect. 4.

2. The dominance of toroidal shapes in hyperheavy $Z \geq 126$ nuclei

The state-of-the-art view on the nuclear landscape is presented in Fig. 1. It is born out of the systematic axial relativistic Hartree–Bogoliubov (RHB) calculations of Refs. [3, 10, 11] supplemented by triaxial RHB calculations for the ground states and fission barriers of selected set of the nuclei [10, 11]. These calculations are based on the DD-PC1 functional [13] which is one of the best CEDFs [3]. For the $Z < 100$ nuclei, we see the classical nuclear structure with pronounced spherical shell gaps at particle numbers 8, 20, 28, 50, 82 (and $N = 126$) leading to the bands (shown by gray color) of spherical nuclei in the nuclear chart along the vertical and horizontal lines with these particle numbers. In addition, the traditional picture of the transition from spherical shapes to prolate ones, then to oblate ones and, finally, to spherical shapes on moving from one spherical shell closure to another one is seen for these nuclei.

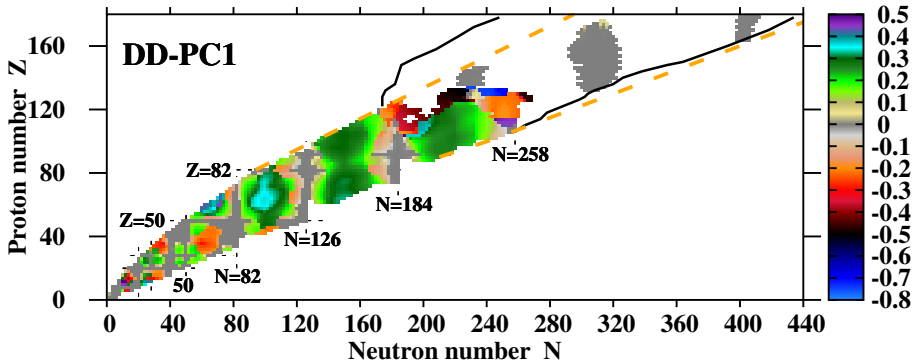


Fig. 1. (Color online) The distribution of ellipsoidal and toroidal shapes in nuclear landscape. The nuclei with ellipsoidal shapes are shown by the squares the color of which indicates the equilibrium quadrupole deformation β_2 (see colormap). Note that ellipsoidal shapes with the heights of fission barriers smaller than 2.0 MeV are considered as unstable (see the discussion in Sect. III of Ref. [14]). Two-proton and two-neutron drip lines for toroidal nuclei are shown by solid black lines. The white region between them (as well as the islands inside this region shown in gray) corresponds to the nuclei which have toroidal shapes in the lowest in energy minimum for axial symmetry (LEMAS). The islands of relatively stable spherical hyperheavy nuclei in the $Z > 130$ nuclei, shown in light gray color, correspond to the solutions which are excited in energy with respect of the LEMAS corresponding to toroidal shapes. Note that in the same nucleus, two-neutron drip lines for spherical and toroidal shapes are different. This is the reason why some islands of stability of spherical hyperheavy nuclei extend beyond the two-neutron drip line for toroidal shapes. The extrapolations of the two-proton and two-neutron drip lines for ellipsoidal shapes, defined from their general trends seen in the $Z < 120$ nuclei, are displayed by thick dashed orange lines.

However, these features are in general gone for superheavy ($Z = 100$ – 124) nuclei. In this region, normal- and super-deformed oblate shapes become dominant for high- Z nuclei (see Fig. 1). Further increase of proton number triggers the transition to toroidal shapes¹. This transition is driven by Coulomb repulsion: for high- Z systems, the Coulomb energy is significantly larger for the ellipsoidal shapes than for toroidal ones (see discussion in Sec. XII of Ref. [11]). As a consequence, the toroidal shapes, correspond-

¹ Many features of toroidal shapes in nuclear physics are discussed in Ref. [15] but these discussions do not extend to hyperheavy nuclei. In recent years, there is an increased interest to toroidal high-spin isomers (see, for example, Refs. [16–18]).

ing to large negative values of the β_2 quantity² become energetically favored as compared with ellipsoidal ones in the nuclei with high- Z values. This is illustrated in Fig. 2 where the competition of three local minima with $\beta_2 \sim -0.8$, $\beta_2 \sim -2.3$, and $\beta_2 \sim -3.8$ are clearly seen. The first minimum corresponds to biconcave disk (oblate) shapes, while other two to toroidal shapes. Dependent on the combination of proton and neutron numbers, one of these minimum becomes LEMAS. In lower- Z nuclei, the biconcave disk shape corresponds to LEMAS (see Fig. 1). The LEMAS in the nuclei in the vicinity of the $Z \sim 136, N \sim 210$ corresponds to toroidal shapes with $\beta_2 \sim -2.3$ (Fig. 2(c) and Ref. [19]). Going away from this region favors toroidal shapes with substantially larger (in absolute value) β_2 quantities (Fig. 2(a) and Ref. [19]). Typical density distributions corresponding to these shapes are shown at the top of Fig. 3.

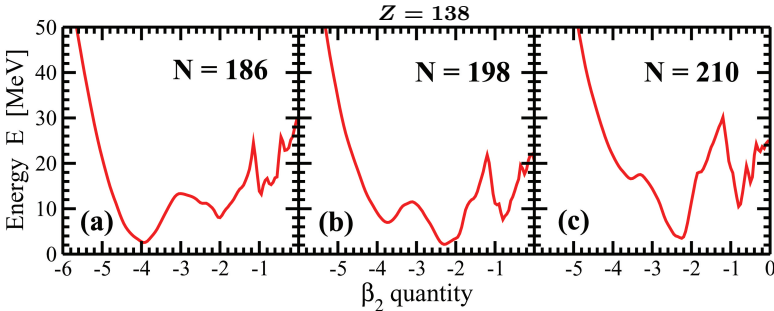


Fig. 2. Deformation energy curves of selected $Z = 138$ hyperheavy nuclei obtained in axial RHB calculations with the DD-PC1 functional.

² The β_2 and γ quantities are extracted from respective quadrupole moments

$$Q_{20} = \int d^3r \rho(\vec{r}) (2z^2 - x^2 - y^2), \quad (1)$$

$$Q_{22} = \int d^3r \rho(\vec{r}) (x^2 - y^2), \quad (2)$$

via

$$\beta_2 = \sqrt{\frac{5}{16\pi}} \frac{4\pi}{3AR_0^2} \sqrt{Q_{20}^2 + 2Q_{22}^2}, \quad (3)$$

$$\gamma = \arctan \sqrt{2} \frac{Q_{22}}{Q_{20}}, \quad (4)$$

where $R_0 = 1.2A^{1/3}$. Note that $Q_{22} = 0$ and $\gamma = 0$ in axially symmetric RHB calculations. The β_2 and γ values have a standard meaning of the deformations only for ellipsoid-like density distributions with $|\beta_2| \lesssim 1.0$. For toroidal shapes ($\beta_2 \lesssim -1.2$), they should be treated as dimensionless and particle normalized measures of the Q_{20} and Q_{22} moments of the density distributions. The β_2 quantity defines the radius R of the toroid and its tube radius d : with increasing absolute value of the β_2 quantity, R increases and d decreases. The γ quantity defines the deviation of the density distribution from symmetric ($\gamma = 60^\circ$) toroid.

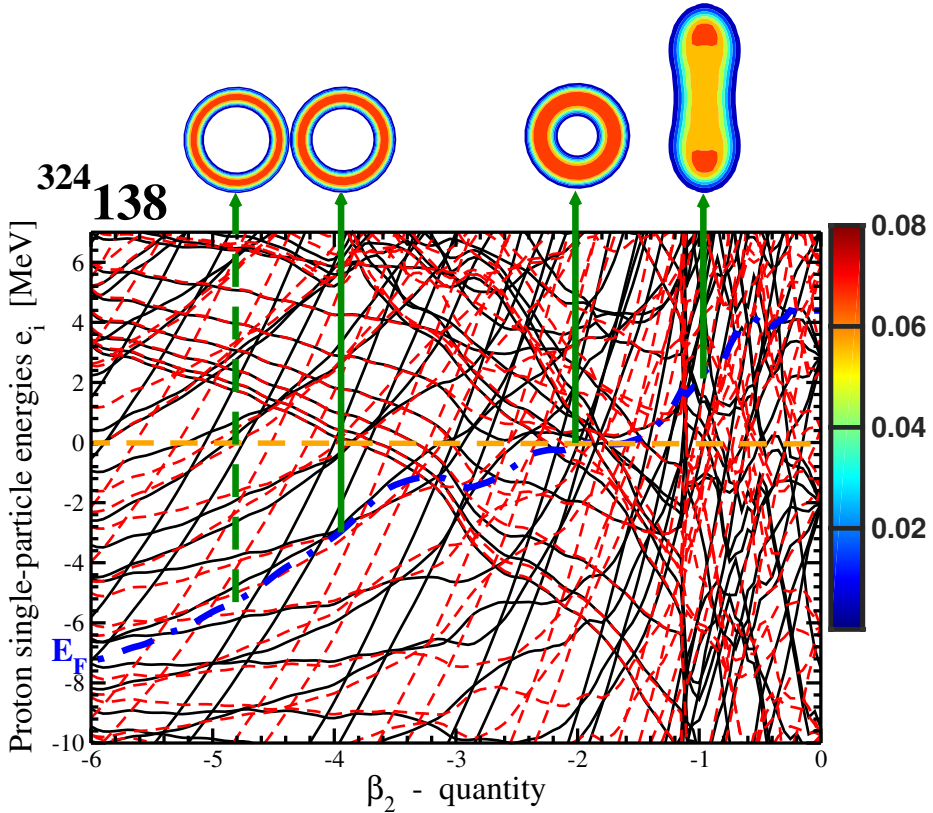


Fig. 3. (Color online) Proton single-particle energies for the lowest in total energy solution in the nucleus $^{324}_{138}$ calculated as a function of the β_2 quantity. Solid and dashed lines are used for positive- and negative-parity states, respectively. Proton density distributions, corresponding to local minima shown in Fig. 2 (a) as well as to the solution with $\beta_2 = -4.8$, are displayed at the top of the figure. They are shown in the plane containing toroid for toroidal shapes and in the plane containing the axis of symmetry for biconcave disk. The density colormap starts at $\rho_n = 0.005 \text{ fm}^{-3}$ and shows the densities in fm^{-3} . Dot-dashed blue and dashed orange lines are used for the Fermi level E_F and zero energy, respectively.

Figure 1 compares the extrapolations of the two-neutron and two-proton drip lines for ellipsoidal shapes with those obtained for toroidal nuclei. Note that these extrapolations are quite close to respective drip lines obtained for the islands of spherical hyperheavy nuclei. The calculated two-neutron drip line for toroidal shapes is close to the extrapolation of this line for ellipsoidal shapes. On the contrary, the situation is completely different on the proton-rich side of the nuclear landscape: the transition to toroidal shapes in the $Z > 120$ nuclei creates a substantial expansion (the area between solid black

and dashed orange lines in Fig. 1) of the nuclear landscape. The reason for that is clearly seen in Fig. 3 on the example of the $^{324}_{138}$ nucleus. The Fermi level E_F for ellipsoidal-like shapes is located at positive energies and thus such shapes are unstable against proton emission. On the contrary, the transition to toroidal shapes drastically modifies the underlying single-particle structure and, as a consequence, lowers the energy of the Fermi level with increasing absolute value of the β_2 quantity. As a consequence, $E_F \approx -3.5$ MeV for LEMAS with $\beta_2 \sim -4.0$ in this nucleus and thus this state is particle bound.

The triaxiality plays a critical role in the demise of ellipsoidal shapes and the emergence of toroidal shapes as a major player in hyperheavy nuclei. This is because the impact of triaxiality on fission barriers gets much more pronounced in the nuclei with ground-state oblate shapes and it generally increases with the rise of their oblate deformation [10, 11]. Not only the fission through the γ -plane gets more energetically favored, but also the fission path through γ -plane becomes much shorter than the one through the $\gamma = 0^\circ$ axis. These features are illustrated in Fig. 4 on few $Z = 134$ nuclei distributed equidistantly in neutron number along the isotopic chain. Let us consider the $^{392}_{134}$ nucleus as an example. In axial RHB calculations, its ground state and excited (at excitation energy of 2.69 MeV) minima are located at $\beta_2 = -0.79$ and $\beta_2 = -0.23$, respectively. The fission barriers for these two minima are 10.24 and 7.55 MeV, respectively. The inclusion of the triaxiality reduces these fission barriers down to 0.56 and 2.08 MeV making ellipsoidal shapes unstable with respect of fission. Similar effects are also seen in the $^{352}_{134}$, $^{372}_{134}$, $^{412}_{134}$ (see Fig. 4) and $^{432}_{134}$ (see Ref. [10]) nuclei. Note that similar trend of substantial reduction of fission barriers for ellipsoidal shapes in hyperheavy nuclei due to triaxiality is seen also in microscopic+macroscopic and Skyrme DFT calculations [20].

The investigation of potential stability of toroidal nuclei with respect of different types of distortions is one of important aspects of their studies. The results of systematic axial RHB calculations of Refs. [10, 11] clearly indicate that toroidal nuclei are stable with respect of breathing deformation³. Note that breathing deformation preserves the azimuthal symmetry of the torus and it is defined by the radius of torus and the radius of its tube [15]. Another type of the distortions of toroidal shapes is with respect of so-called sausage deformations; they make a torus thicker in one section(s) and thinner in another section(s) [15]. Such a distortion, corresponding to sausage deformation of the order of $\lambda = 2$, is exemplified in Fig. 5 as the transition from the density distribution shown in panel (a) to that shown in panel (b). The study of such deformations requires triaxial RHB or RMF+BCS com-

³ Similar results have also been obtained in the HFB calculations with the Gogny force but only for two nuclei [21].

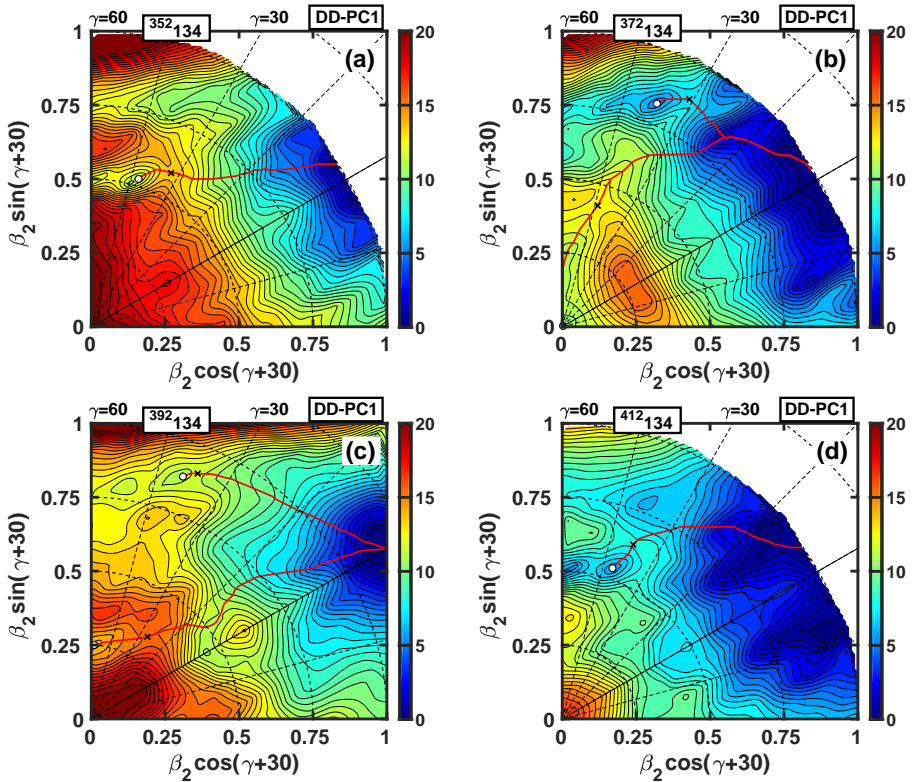


Fig. 4. (Color online) Potential energy surfaces (PES) of indicated nuclei obtained in the RHB calculations. The energy difference between two neighboring equipotential lines is equal to 0.5 MeV. The solid red lines show static fission paths from respective minima. Open white circles show the global (and local) minimum(a). Black crosses indicate the saddle points on these fission paths. The colormap shows the excitation energies (in MeV) with respect to the energy of the deformation point with largest binding energy. The panel with the results for $^{392}_{134}$ nucleus is taken from Ref. [10].

puter codes and could be potentially performed only for toroidal shapes in the $Z \sim 134, N \sim 210$ region, which are characterized by small radius of torus and large radius of its tube, because of enormous requirements on the basis size (see Sect. III in Ref. [11]). Even then such calculations are extremely time-consuming. As a result, the stability of toroidal hyperheavy nuclei with respect of non-axial distortions related to sausage deformations of the order of $\lambda = 2$ has been studied so far for only two nuclei, namely, $^{354}_{134}$ and $^{348}_{138}$ in Refs. [10, 11]. The saddle points of their fission barriers with respect of such distortions are located at 4.4 and 8.54 MeV, respectively; this is indicative of their potential stability.

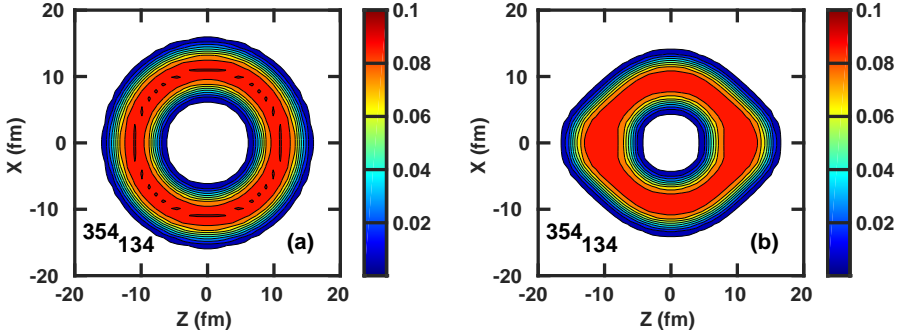


Fig. 5. (Color online) Neutron density distributions of the lowest stable toroidal configuration with $\beta_4 \sim 1.5$ in the $^{354}_{134}$ nucleus corresponding to its minimum with $\beta_2 \sim 2.3, \gamma = 60^\circ$ (left panel) and the saddle with $\beta_2 \sim 2.0, \gamma \approx 35^\circ$ (right panel). The density colormap starts at $\rho_n = 0.005 \text{ fm}^{-3}$ and shows the densities in fm^{-3} .

The situation with odd order sausage deformations with $\lambda = 1$ and 3 is even more complicated because its resolution requires the use of spatial symmetry unrestricted computer codes. However, numerical calculations with basis sizes following from the analysis of Sect. III of Ref. [11] are impossible nowadays in such computer codes.

3. Extension of nuclear landscape by means of rotational excitations

Two new mechanisms active in rotating nuclei located in the vicinity of neutron drip line have been discovered by us in Ref. [12]. This investigation has been performed in the cranked relativistic mean field (CRMF) approach [22, 23] without pairing; the neglect of pairing is a reasonable approximation for high spins of interests (see Ref. [12] for details). The strong Coriolis interaction acting on high- j orbitals transforms particle-unbound (resonance) nucleonic configurations into particle-bound ones with increasing angular momentum. The point of the transition manifests *the birth of particle-bound rotational bands*. This mechanism is best illustrated on the example of the $[3,0]^4$ configuration in the ^{46}Mg neutron routhian diagram which is shown in Fig. 6.

The $3/2[431](r = -i)$ orbital is the highest in energy occupied positive parity intruder orbital in this configuration. In each (proton or neutron) subsystem, the energy of the highest occupied orbital corresponds to the

⁴ This configuration contains 3 neutrons in the intruder $N = 4$ orbitals and no protons in the intruder $N = 3$ orbitals; see Ref. [12] for more details.

energy of the Fermi level in the calculations without pairing [24]. Thus, the nucleonic configuration, the energy of the last occupied neutron orbital of which is negative, is expected to be particle bound. At rotational frequency $\Omega_x < 1.03$ MeV, the $3/2[431](r = -i)$ orbital is particle unbound since its single-particle energy is positive (see Fig. 6). Thus, at low spin (up to $I \sim 16\hbar$ corresponding to $\Omega_x = 1.03$ MeV), the rotational band built on this configuration can exist only as a band embedded in particle continuum (see Refs. [25, 26]) (further ‘resonance band’). Above this frequency, its energy becomes negative and this orbital dives (because of its high- j content leading to strong Coriolis force) deeper into nucleonic potential with increasing rotational frequency. As a consequence, the $[3,0]$ configuration becomes particle bound. Thus, respective rotational band changes its character from particle-unbound resonance band (at $I < 16\hbar$) to particle-bound rotational band (at $I > 16\hbar$) with discrete rotational states of extremely narrow width. Alternative possibility of the transition from particle-bound to resonance rotational band (*the death of particle-bound rotational bands*⁵) with increasing spin also exists but it is less frequent in the calculations.

The birth of particle-bound rotational bands provides a mechanism for the extension of nuclear landscape to neutron numbers which are larger than those of the neutron drip line in non-rotating nuclei (Ref. [12]). For example, at spin zero, ^{46}Mg is the last bound even–even nucleus [3]. However, neutron bound rotational states are predicted at non-zero spins also in $^{48,50}\text{Mg}$ which are unbound at spin zero (see Figs. 6 (i) and (j) in Ref. [12]). Thus, rotational excitations allow to extend the nuclear landscape for the Mg isotopes by four neutrons.

On-going investigation [29] reveals that similar mechanisms are active also in the nuclei in the vicinity of proton drip line. However, in this case, the birth of particle (proton) bound rotational bands and the extension of nuclear landscape beyond spin-zero proton drip line⁶ emerge from proton intruder orbitals initially located at positive energies which, with increasing rotational frequency, dive into negative energy domain because of high- j angular momentum content leading to a large Coriolis force. However, due to the presence of the Coulomb barrier, the part of the rotational band with

⁵ The stability of aligned states in the ^{40}Ca , ^{66}Ge , ^{122}Xe and ^{150}Gd nuclei with increasing spin has been studied in Ref. [27]; above some spin value, such states become particle unstable. Despite some similarities of our results and those of Ref. [27], there are important differences. We consider collective rotation of the nuclei, while the regime of nuclear motion in aligned states of Ref. [27] corresponds to a so-called “non-collective rotation” (see Refs. [24, 28]). These aligned states in many cases represent non-collective terminating states of rotational bands (or highest spin state within a rotational band) [28].

⁶ See Refs. [2, 3, 7] for the state-of-the-art predictions of the position of proton drip line.

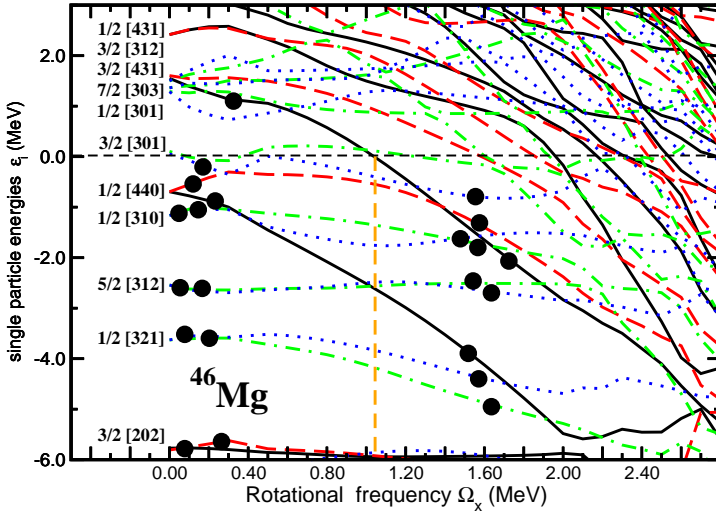


Fig. 6. (Color online) Neutron single-particle energies (routhians) in the self-consistent rotating potential of ^{46}Mg as a function of rotational frequency Ω_x . They are given along the deformation path of the $[3,0]$ configuration. Long-dashed red, solid black, dot-dashed green, and dotted blue lines indicate $(\pi = +, r = +i)$, $(\pi = +, r = -i)$, $(\pi = -, r = +i)$, and $(\pi = -, r = -i)$ orbitals, respectively. At $\Omega_x = 0.0$ MeV, the single-particle orbitals are labeled by the asymptotic quantum numbers $\Omega[Nn_zA]$ (Nilsson quantum numbers) of the dominant component of the wave function. Solid circles indicate occupied orbitals in resonance and particle-bound parts of respective configurations. Vertical dashed orange line indicates the frequency at which the configuration becomes particle bound.

at least one occupied proton single-particle state having positive energy will have discrete rotational states which can decay also by proton emission. This is contrary to the situation near neutron drip line where occupied neutron state(s) with positive energy result in resonance part of the band with rotational states having finite width. The nucleonic configuration will be proton bound for the case of negative energy of highest occupied proton orbital. Similar to very neutron-rich nuclei, the dive of intruder proton orbitals into nucleonic potential can trigger the transition from proton emitting part of rotational band at low spin to proton bound one at higher spin.

These features are illustrated in Figs. 7 and 8. The ^{50}Ni and ^{48}Ni are the last proton bound and the first proton unbound Ni nuclei at spin zero [3]. At $I = 0$, these nuclei are spherical due to the presence of the $Z = 28$ and $N = 20$ shell closures. However, particle-hole excitations across these gaps lead to the development of large and extreme deformations (see Ref. [30]) as well as to the occupation of positive energy proton orbitals in excited

configurations. As a consequence, these bands are proton emitting. However, some configurations built on intruder proton orbitals, such as [0,2] and [2,42] in ^{50}Ni and [0,2] in ^{48}Ni , which are proton emitting at low and moderate spins become proton bound at high spins. The underlying microscopic mechanism is illustrated in Fig. 8. Proton $1/2[440](i = \pm)$ intruder orbitals, occupied in the [0,2] configuration of ^{48}Ni , are located at positive energy at low spins. However, both of them dive into negative energy domain with increasing rotational frequency so that the [0,2] configuration become particle bound at $\Omega_x = 2.04 \text{ MeV}$ ($I \approx 26\hbar$).

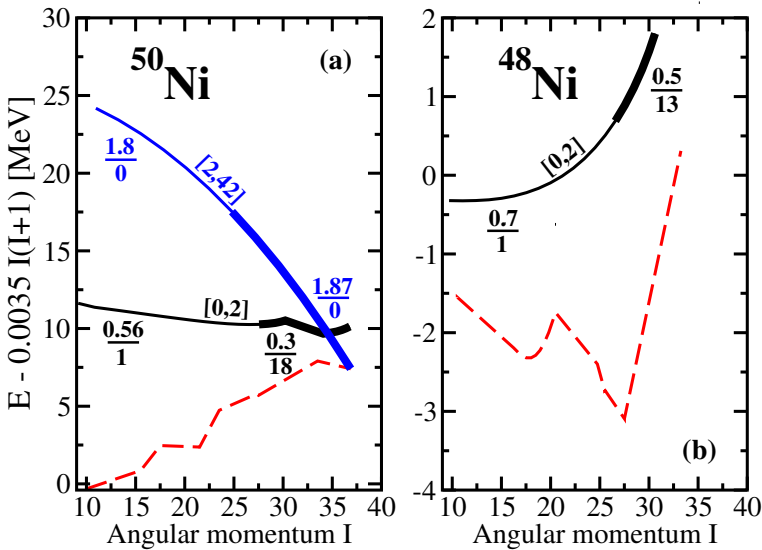


Fig. 7. (Color online) Excitation energies of calculated configurations in $^{48,50}\text{Ni}$ relative to a rotating liquid drop reference $AI(I + 1)$, with the inertia parameter $A = 0.0035$. Thin and thick lines show proton emitting and proton bound parts of rotational bands, respectively. The yrast lines (as defined from approximately 15 calculated configurations) are shown by dashed red lines. Typical deformations of the bands are shown in the format of $\frac{\beta_2}{\gamma}$. The configurations in proton-rich Ni isotopes are labeled by the shorthand $[n_1, p_1(p_2)]$ labels, where n_1 is the number of neutrons in the intruder $N = 4$ orbitals, and p_1 and p_2 are the number of protons in the $N = 4$ intruder and $N = 5$ hyperintruder orbitals. The p_2 number is omitted when respective orbitals are not occupied.

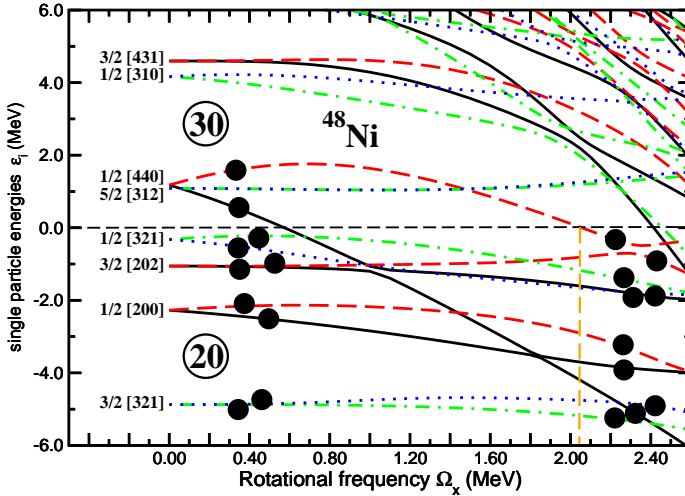


Fig. 8. (Color online) The same as Fig. 6 but for proton routhians in the $[0,2]$ configuration of ^{48}Ni .

4. Conclusions

In conclusion, it was illustrated that traditional limits of nuclear landscape can be substantially expanded when considering the mechanisms alternative to those discussed before. In the region of hyperheavy nuclei, the transition from ellipsoid-like nuclear shapes to toroidal ones provides a substantial increase of nuclear landscape. Rotational excitations provide an alternative mechanism of the extension of nuclear landscape beyond the limits defined at spin zero. In both cases, the collective coordinates related to nuclear shapes play an important role in extending nuclear landscape. In hyperheavy nuclei, they drive the nuclear systems from ellipsoidal-like to toroidal shapes. In rotating nuclei, they transform the system from spherical or normal deformed ground states to extremely elongated (super-, hyper- and mega-deformed) shapes at high spins. This creates favorable positions of intruder orbitals with respect of zero energy threshold which combined with the action of collective rotation allows to extend the limits of nuclear landscape beyond spin-zero ones.

This material is based upon work supported by the U.S. Department of Energy, Office of Science, Office of Nuclear Physics under Award No. DE-SC0013037 and the U.S. Department of Energy, National Security Administration under Award No. DE-NA0002925.

REFERENCES

- [1] D. Vretenar, A.V. Afanasjev, G.A. Lalazissis, P. Ring, *Phys. Rep.* **409**, 101 (2005).
- [2] A.V. Afanasjev, S.E. Agbemava, D. Ray, P. Ring, *Phys. Lett. B* **726**, 680 (2013).
- [3] S.E. Agbemava, A.V. Afanasjev, D. Ray, P. Ring, *Phys. Rev. C* **89**, 054320 (2014).
- [4] A.V. Afanasjev, S.E. Agbemava, *Phys. Rev. C* **93**, 054310 (2016).
- [5] J. Dobaczewski, W. Nazarewicz, P.-G. Reinhard, *J. Phys. G: Nucl. Part. Phys.* **41**, 074001 (2014).
- [6] A.V. Afanasjev, S.E. Agbemava, D. Ray, P. Ring, *Phys. Rev. C* **91**, 014324 (2015).
- [7] J. Erler *et al.*, *Nature* **486**, 509 (2012).
- [8] S.E. Agbemava, A.V. Afanasjev, A. Taninah, *Phys. Rev. C* **99**, 014318 (2019).
- [9] Y. Gao *et al.*, *Phys. Rev. C* **87**, 034324 (2013).
- [10] A.V. Afanasjev, S.E. Agbemava, A. Gyawali, *Phys. Lett. B* **782**, 533 (2018).
- [11] S.E. Agbemava, A.V. Afanasjev, A. Taninah, A. Gyawali, *Phys. Rev. C* **99**, 034316 (2019).
- [12] A.V. Afanasjev, N. Itagaki, D. Ray, *Phys. Lett. B* **794**, 7 (2019).
- [13] T. Nikšić, D. Vretenar, P. Ring, *Phys. Rev. C* **78**, 034318 (2008).
- [14] H. Abusara, A.V. Afanasjev, P. Ring, *Phys. Rev. C* **85**, 024314 (2012).
- [15] C.Y. Wong, *Ann. Phys.* **77**, 279 (1973).
- [16] A. Staszczak, C.-Y. Wong, *Phys. Lett. B* **738**, 401 (2014).
- [17] A. Staszczak, C.-Y. Wong, A. Kosior, *Phys. Rev. C* **95**, 054315 (2017).
- [18] T. Ichikawa, K. Matsuyanagi, J.A. Maruhn, N. Itagaki, *Phys. Rev. C* **90**, 034314 (2014).
- [19] S.E. Agbemava, A.V. Afanasjev, in preparation.
- [20] W. Brodziński, J. Skalski, *Phys. Rev. C* **88**, 044307 (2013).
- [21] M. Warda, *Int. J. Mod. Phys. E* **16**, 452 (2007).
- [22] W. Koepf, P. Ring, *Nucl. Phys. A* **511**, 279 (1990).
- [23] A.V. Afanasjev, H. Abusara, *Phys. Rev. C* **82**, 034329 (2010).
- [24] S.G. Nilsson, I. Ragnarsson, «Shapes and Shells in Nuclear Structure», *Cambridge University Press*, 1995.
- [25] E. Garrido, A.S. Jensen, D.V. Fedorov, *Phys. Rev. C* **88**, 024001 (2013).
- [26] K. Fossef *et al.*, *Phys. Rev. C* **93**, 011305 (2016).
- [27] M. Cerkaski *et al.*, *Phys. Lett. B* **72**, 149 (1977).
- [28] A.V. Afanasjev, D.B. Fossan, G.J. Lane, I. Ragnarsson, *Phys. Rep.* **322**, 1 (1999).
- [29] A. Taninah, A.V. Afanasjev, in preparation.
- [30] A.V. Afanasjev, D. Ray, *Phys. Rev. C* **94**, 014310 (2016).